Computational Nanomechanics of Quasi-one-dimensional Structures in a Symmetry-Adapted Tight Binding Framework

Traian Dumitrica

Abstract The success of many nanotechnologies depends on our ability to understand and control the mechanics of nano objects, such as nanotubes and nanobelts. Because of the numerous experimental difficulties encountered at this scale, simulation can emerge as a powerful predictive tool. For this, new multiscale simulation methods are needed in which a continuum model emerges from a precise, quantum mechanical description of the atomic scale. Because computing nanomechanical responses requires large systems, computationally affordable but less accurate classical atomistic treatments of the atomic scale are widely adopted and only multiscale classical atomistic-to-continuum bridging is achieved. As a first step towards achieving accurate multiscale models for nano objects, based on a quantum-mechanical description of chemical bonding, here we present an ingenious symmetry-adapted atomistic scheme that performs calculations under helical boundary conditions. The utility of the microscopic method is illustrated with examples discussing the nanomechanical response of carbon nanotubes and thermodynamical stability of silicon nanowires.

1 Introduction

The discovery of quasi one-dimensional organizations of matter with distinct shapes – nanotubes [1, 2], and nanowires [3, 4] – opened a new frontier in science and engineering. Understanding the behavior of these structures is not only of fundamental but also of practical importance, because by capitalizing on the science emerging from the newly accessible size range, engineers can develop technologies that will benefit humankind. The success of these nanotechnologies depends on our ability to understand and control the nanoscale mechanics. As experimental difficulties are numerous on this small scale, computer simulations emerge as a powerful predictive tool with great effects on technological innovation.

T. Dumitrica (✉)
Department of Mechanical Engineering, University of Minnesota, Saint Paul, MN, USA
e-mail: td@me.umn.edu

A. Aldea, V. Bârsan (eds.), *Trends in Nanophysics,* Engineering Materials,
DOI 10.1007/978-3-642-12070-1_2,

It should be noted that atomistic simulation methods are required at the nanoscale. However, because of the structure of interest extent over several micrometers or more in one direction, a full atomistic treatment is prohibitive. This situation demands new simulation methods and the vision is that nanoscale modeling will be achieved through a multiscale approach, where the continuum emerges from a precise, quantum mechanical description of the atomic scale [5].

The first important step to achieve multiscale modeling is designing an atomistic scheme to compute the nanomechanical response with high accuracy. Based on the obtained result, one can further construct a continuum model of the nano objects. The chapter is addressing this first critical step by presenting a *symmetry-adapted microscopic modeling approach* applicable to a large class of quasi one-dimensional nanostructures.

Since computing nanomechanical response requires relatively large systems (at least a few hundred of atoms), computationally affordable but less accurate classical atomistic treatments of the atomic scale are heavily adopted [6–11]. To date, only multiscale classical atomistic-to-continuum bridging is achieved [12–19]. Unfortunately, the inaccuracy of the "parent" atomistic model directly transfers to the continuum one and this severely limits our predictive power. The accurate atomistic tools to study the properties of matter are the methods that explicitly account for the quantum mechanics of the electrons. Originally developed in the context of quantum chemistry and condensed matter physics, these powerful methods combine fundamental quantum-mechanical predictive power with atomic resolution in length and time. These methods include density-functional theory [20–22] and tight binding [23, 24] molecular dynamics.

An accurate atomistic description is highly desirable in computational nanomechanics. In order to deliver quantitative prediction, suited for further engineering use, the accurate quantum-mechanical description of chemical bonding is needed. Furthermore, because the electronic subsystem is treated explicitly, electronic, optical or piezoelectric properties can be also derived. Unfortunately, the size range covered by quantum-mechanical methods (of a few hundred atoms) is the major impediment for using these methods in nanomechanics. (This is in spite of the face that the size limit increases rapidly due to parallel computing.)

This work does not intend to advance nanomechanics by trying to enlarge the current computational limit for number of atoms that can be treated with quantum mechanical accuracy. Instead, within the current computational limits, the main idea is to introduce a substantial simplification in the atomistic computations by making recourse to the helical symmetry of the nano objects.

The concept is illustrated in Fig. 1 for a single walled carbon nanotube structure, which can be viewed as the result of rolling up into a seamless tube a flat sheet of graphite, called graphene. The hexagonal structure of graphene, see Fig. 1a, is described by translating a two-atom cell (orange shaded) along the lattice vectors $\mathbf{T_1}$ and $\mathbf{T_2}$. Rolling into a tube can be performed under various curvatures in different directions. For example, Fig. 1b shows a chiral tube obtained by rolling the graphene along the circumference vector $\mathbf{C}$ having distinct components (6 and 3, respectively) along $\mathbf{T_1}$ and $\mathbf{T_2}$. Through folding, the $\mathbf{T_1}$ and $\mathbf{T_2}$ directions wind up in helixes. To

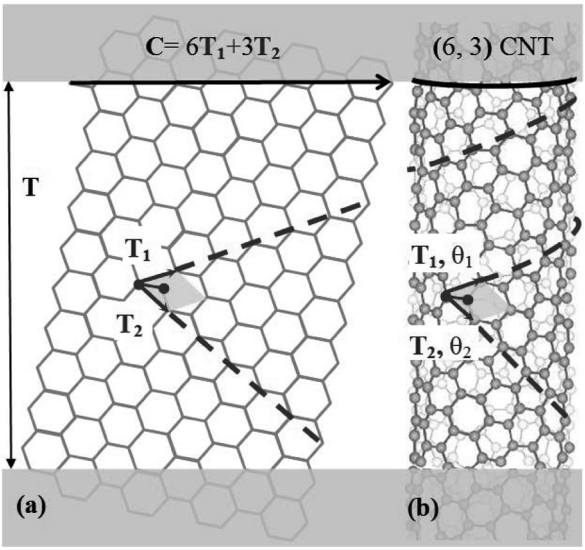

Fig. 1 Translational cell of a (6,3) nanotube in the (**a**) unfolded and (**b**) folded representation

describe the resulting tube structure, one must apply both translations ($\mathbf{T_1}$ and $\mathbf{T_2}$) and rotations (θ_1 and θ_2) around the tube axis to a two-atom cell.

When computing properties of a system with crystalline order, current implementations operating under periodic boundary condition, make recourse to the specific translational symmetry of the structure to simplify the problem to the extent that microscopic calculations are performed on the small translational repeating cells. For example, to obtain bulk properties of graphene (Fig. 1a), a calculation on the two-atom unit cell suffices [25]. However, in a system with helical symmetry the translational periodicity doesn't bring the same advantage. For example, Fig. 1b shows that the translational cell of a chiral nanotube (with axial periodicity T) contains a large number of atoms. Often such translational cells are even too large to allow a quantum treatment. However, calculations would become as convenient as in the flat graphene, if one can take advantage of the helical symmetry and further reformulate the problem with augmented repetition rule to include translations and rotations.

The use of helical symmetry at the nanoscale is very much in its infancy. To date, it has attracted the interest of the research community working on carbon nanotubes [26–28]. Fortunately, the type of simplification portrayed in Fig. 1 actually applies to a large category of quasi one-dimensional nanostructures, recently called objective structures [29, 30].

In the first part, our main objective is to outline the tight binding computational tool able to operate under the new helical boundary condition. We will call symmetry-adapted modeling, the new scheme that operates under helical boundary condition. It is not necessary to create this capability from scratch. Instead, the strategy is to implement the new helical boundary condition into an existing tight binding

solver, now able to operate with the translational periodic boundary conditions. We detail the necessary steps that were undertaken to modify the existing computational package *Trocadero* [31]. By using this code we inherited important features such as atomistic models for various chemical elements as well as numerical algorithms (such as dynamics under constant temperature) that can be immediately used in conjunction with the new symmetry-adapted boundary conditions.

In the second part, our goal is to illustrate how the created computational capability can be used to obtain the accurate modeling and the nanomechanical response of carbon nanotubes and silicon nanowires. Besides the immediate interest, these results are of great interest for multiscale modeling since such data is needed to construct and validate continuum models. (However, this aspect is beyond the scope of the present chapter.)

2 Methodology

2.1 Tight Binding Preliminaries

Tight binding is a basic semi-empirical method which offers a satisfying description of the electronic structure and bonding of covalent systems in an intuitive localized picture. The tight-binding method of modelling materials lies between the very accurate, very expensive, ab initio methods and the fast but limited *empirical* methods. When compared with ab initio methods, tight binding is typically two to three orders of magnitude faster, but suffers from a reduction in transferability due to the approximations made; when compared with *empirical* methods, tight binding is two to three orders of magnitude slower, but the quantum mechanical nature of bonding is retained, ensuring that the angular nature of bonding is correctly described far from equilibrium structures. Tight binding is therefore useful for the large number of situations in which quantum mechanical effects are significant, but the system size makes ab initio calculations impractical. More specifically, with relatively modest resources up to about 500 atoms can be comfortably treated with tight binding.

Invoking the Born-Oppenheimer approximation, from the electronic structure one can extract a tight binding potential that can be used to carry out tight binding molecular dynamics simulations.

2.1.1 Formulation of Tight Binding Molecular Dynamics in a One-Dimensional Bravais Lattice

In tight binding the electronic states of a periodic structure are obtained by solving the one-electron Schrödinger equation

$$\left[-\frac{\hbar^2}{2m}\nabla^2 + V(\mathbf{r})\right]|j\rangle = \varepsilon_j|j\rangle, \tag{1}$$

where m is the electron mass, $\hbar$ the Plank's constant, $V(\mathbf{r})$ an effective periodic potential, and $|j\rangle$ and ε_j are the one-electron wavefunction and energy for the state j, respectively. This equation is solved with the ansatz that the single electron states can be represented in terms of atomic orbitals located on each single atom. The number of atomic orbitals n_α is usually taken equal with the number of valence electrons for the atomic species (for example $n_\alpha = 4$ for carbon and silicon). Let N_t (usually a large number) the number of translational cells over which periodic boundary condition are imposed and let N_0 be the number of atoms in each cell. If no explicit recourse to translational symmetry is made, the one-electron eigenfunctions $|j\rangle$ are represented in terms of localized orbitals functions $|\alpha n\rangle$, where α labels the orbital symmetry (s, p_x, p_y, p_z for our case) and n the atomic location:

$$|j\rangle = \sum_{\alpha,n} C_{\alpha n}(j)|\alpha n\rangle, \quad j = 1, ..., N. \tag{2}$$

The number of eigenstates $N = n_\alpha \cdot N_0 \cdot N_t$ equals the total number of valence electrons in the N_t translational cells considered. The expansion coefficients grouped in the vector $\mathbf{C}(j)$ should be obtained from the one-electron generalized $N \times N$ eigenvalue problem

$$\mathbf{H} \cdot \mathbf{C}(j) = \varepsilon_j \mathbf{S} \cdot \mathbf{C}(j), \ j = 1, \ldots, N, \tag{3}$$

which can be easily obtained by substituting Eq. (2) into (1). Equation (3) is known as the matrix form of the Schrödinger equation. In tight binding, the matrix the elements of the Hamiltonian $\mathbf{H}$ matrix – e^0_α diagonal and $t^0_{\alpha',\alpha}$ off-diagonal – and of the overlap $\mathbf{S}$ matrix $s^0_{\alpha',\alpha}$ are not explicitly calculated. They are replaced with a parameter which depends only on the internuclear distance and the symmetry of the orbitals involved. The parameterization is performed by using the available experimental data or by making recourse to more accurate but computationally expensive *first principles* [32, 33] calculations.

The total energy contained in the electronic states writes:

$$E_{\text{band}} = 2 \sum_{j=1}^{N} f_j \varepsilon_j, \tag{4}$$

where f is the Fermi distribution function.

2.1.2 Tight Binding Under Periodic Boundary Condition – The Electronic Structure

Of course, in a crystalline structure with N on the order of 10^{23}, the $N \times N$ eigenvalue problem (3) cannot be solved directly. The usual approach is to introduce a significant computational simplification by explicitly accounting for the *translational*

symmetry. For simplicity, we are next presenting this approach only for the one-dimensional crystal. (The expansion to the three-dimensional case is trivial.)

Let $\mathbf{T}$ be the lattice periodicity vector and $\{\mathbf{X}_n : n = 1, \ldots, N_0\}$ the atomic positions within the unit cell. The atomic locations in one-dimensional periodic structure can be obtained with

$$\mathbf{X}_{n,\zeta} = \zeta \mathbf{T} + \mathbf{X}_n, \tag{5}$$

where $\zeta = 0, \ldots, N_t - 1$, and $n = 1, \ldots, N_0$. To incorporate the translational symmetry, instead of Eq. (2) the one-electron solutions are represented in terms of the Bloch sums:

$$|\alpha n, k\rangle = \frac{1}{\sqrt{N_t}} \sum_{\zeta} e^{ikT\zeta} |\alpha n, \zeta\rangle, \tag{6}$$

where the wavenumber k takes N_t uniformly spaced values in the interval $-\pi/T \leq k < \pi/T$, with $\delta k = 2\pi/TN_t$. $|\alpha n, \zeta\rangle$ represents the orbital α located on atom n located in the translational cell ζ, with $\zeta = 1, ..., N_t$. The advantage is that in the representation (6), the tight binding Hamiltonian and overlap matrix elements between two $\langle \alpha n', k'|$ and $|\alpha n, k\rangle$ sums are vanishing unless $k = k'$. Thus, the eigenvalue problem becomes block-diagonal and it can be solved separately for each N_t block labeled by k and having dimension $(N/N_t)\times(N/N_t)$:

$$\mathbf{H}(k) \cdot \mathbf{C}(j, k) = \varepsilon_j(k)\mathbf{S}(k) \cdot \mathbf{C}(j, k), \quad j = 1, ..., N/N_t. \tag{7}$$

In other words, instead of solving the single $N \times N$ eigenvalue problem (3) to obtain the N electronic states, one solves instead N_t eigenvalue problems (7) of size $N/N_t \times N/N_t$ to obtain the same N electronic states, now labeled by j and k.

Formally, in the two-center approximation, the k-dependent elements of Hamiltonian $\mathbf{H}$ and overlap $\mathbf{S}$ matrices write:

$$\langle \alpha' n', k|H|\alpha n, k\rangle = \sum_{\zeta} e^{-ikT\zeta} t^0_{\alpha'\alpha}(\mathbf{X}_{n',\zeta} - \mathbf{X}_n), \tag{8}$$

$$\langle \alpha' n', k|\alpha n, k\rangle = \sum_{\zeta} e^{-ikT\zeta} s^0_{\alpha',\alpha}(\mathbf{X}_{n'\zeta} - \mathbf{X}_n). \tag{9}$$

As before, $\mathbf{X}_n$ represent the atomic coordinates in the initial $\zeta = 0$ cell.

2.1.3 Tight Binding Molecular Dynamics Under Periodic Boundary Condition

In the translational formulation, the total energy contained in the electronic states writes:

$$E_{\text{band}} = 2 \sum_{j=1}^{N/N_t \sum_k^{\delta k(N_t-1)/2} = -\delta k(N_t-1)/2} f_j(k) E_j(k), \tag{10}$$

and depends parametrically on the coordinates of the nuclei. In the framework of the Born-Oppenheimer approximation [34], once the electronic energy is found, it can be directly used to give the motion of the nuclei, which are treated classically. More precisely, to perform molecular dynamics, the forces acting on the N_0 atoms located in the initial cell, are needed. In tight binding molecular dynamics, the force due to the band energy on the atom at $\mathbf{X}_m$ located in the initial cell due to the band energy, $\mathbf{F}_m = -\partial E_{\text{band}}/\partial \mathbf{X}_m$, writes:

$$\mathbf{F}_m = -2 \sum_{j,k} f_j(k) \left(\mathbf{C}^\dagger(j,k) \cdot \frac{\partial \mathbf{H}(k)}{\partial \mathbf{X}_m} \cdot \mathbf{C}(j,k) - \varepsilon_j(k) \mathbf{C}^\dagger(j,k) \cdot \frac{\partial \mathbf{S}(k)}{\partial \mathbf{X}_m} \cdot \mathbf{C}(j,k) \right), \tag{11}$$

which is the Hellmann-Feynman force. Typical derivatives of the tight binding Hamiltonian and overlap matrix elements are:

$$\frac{\partial \langle \alpha' n', \kappa | H | \alpha m, \kappa \rangle}{\partial \mathbf{X}_m} = \frac{1}{N_t} \sum_{\zeta} e^{-i\kappa\zeta} \frac{\partial t^0_{\alpha',\alpha}(\mathbf{X}_{n',(\zeta)} - \mathbf{X}_m)}{\partial \mathbf{X}_m}, \tag{12}$$

$$\frac{\partial \langle \alpha' n', k | \alpha m, k \rangle}{\partial \mathbf{X}_m} = \frac{1}{N_t} \sum_{\zeta} e^{-ik\zeta} \frac{\partial s^0_{\alpha',\alpha}(\mathbf{X}_{n',(\zeta)} - \mathbf{X}_m)}{\partial \mathbf{X}_m}. \tag{13}$$

In tight binding one assumes a form for the Hamiltonian and overlap matrix elements without specifying anything about the atomic orbitals except their symmetry. The values of the matrix elements may be derived approximately or may be fitted to experiment or other theory.

2.2 *Detailed Formulation of the Symmetry-Adapted Tight Binding Molecular Dynamics*

A major disadvantage of tight binding is still its high computational cost: Computing the electronic structure energy and forces from a tight binding Hamiltonian by direct diagonalization results in a cubic scaling of the computational time with the number of electrons considered [$O(N^3)$]. This limits the system size to about 1000 Si or C atoms. In a Bravais lattice, the number of atoms is small. Thus, the above approach is suitable in simulations of bulk crystals. However, the simplifications due to the periodic boundary condition are insufficient for comprehensive calculations of quasi one-dimensional objects such as nanowires and nanotubes. This is because the number of atoms in the translational unit cells can be very large, leading to a large-size matrix equation for the electronic problem. Note that there is a current research line

that attempts to alleviate this notorious dependence of computation time with $O(N)$ methods. However, the errors introduced in the electronic band structure could affect the outcome.

2.2.1 Symmetry-Adapted Tight Binding Molecular Dynamics in the "Angular-Helical" Representation

Figure 1 suggests that the nanotube structures could be described by applying successive commuting helical transformations. However such "helical-helical" representation is not convenient for a quantum mechanical implementation. For this reason, here we introduce the "helical-angular" representation [25].

An infinitely-long CNT exhibits *translational* symmetry. When its unrolled unit cell is projected on the graphene layer, Fig. 2, the circumference turns into the chiral vector $\mathbf{C}_h = l_1\mathbf{a}_1 + l_2\mathbf{a}_2$ of modulus $|\mathbf{C}_h| = a\sqrt{l_1^2 + l_2^2 + l_1 l_2}$. Here a is the lattice constant for the flat honeycomb lattice. The CNT axis aligns to the translational vector $\mathbf{T} = t_1\mathbf{a}_1 + t_2\mathbf{a}_2$, where $t_1 = (2l_2 + l_1)/d_R$ and $t_2 = -(2l_1 + l_2)/d_R$. Here $d_R = \gcd(2l_1 + l_2, 2l_2 + l_1)$, where gcd indicates the greatest common divisor of the two number within the brackets. The length of the translational vector is $|\mathbf{T}| = \sqrt{3}|\mathbf{C}_h|/d_R$. The translational unit cell of the CNT is delineated by $\mathbf{T}$ and $\mathbf{C}_h$. It also follows [25] that the number of carbon pairs inside the translational unit cell writes $N = 2(l_1^2 + l_1 l_2 + l_2^2)/d_R$.

The translational representation of the infinitely long CNT is widely used for computing the elastic response. One disadvantage is that it requires the explicit treatment of all N atoms, and N scales with the CNT's diameter and chirality angle χ. Only a small number of carbon nanotubes (small-diameter and achiral ones) have N computationally affordable for tight binding and density functional theory.

In addition to *translation*, carbon nanotubes exhibit *angular* and *helical* symmetries [25], also conveniently described by vectors in the example of Fig. 2. For *angular* symmetry, note that while $\gcd(t_1, t_2) = 1$ (indicating that $\mathbf{T}$ never spans in the axial direction two identically-oriented carbon pairs), $d = \gcd(l_1, l_2)$ can take any value between 1 and n (supposing that $0 \leq l_2 \leq l_1$). Thus, $\mathbf{C}_h$ spans d

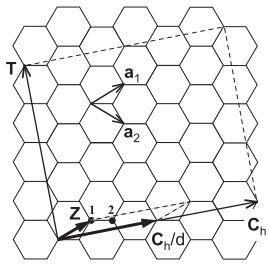

Fig. 2 Unfolded representation of a (4,2) CNT. The big rectangle shows the translational unit cell bounded by the chiral $\mathbf{C}_h$ and translational $\mathbf{T}$ vectors. The small parallelogram shows the "helical-angular" cell bounded by the rotational $\mathbf{C}_h/d$ and screw $\mathbf{Z}$ vectors. It contains atoms 1 and 2. Graphene's lattice vectors $\mathbf{a}_1$ and $\mathbf{a}_2$ are also shown

identically-oriented carbon pairs in the circumferential direction and the rotation vector is given by $\mathbf{C}_h/d$. For *helical* symmetry, we note that among the $N-1$ non-equivalent vectors connecting the graphene lattice points within the translational unit cell, $d-1$ correspond to pure angular rotations, while the remaining $N-d$ correspond to distinct screw operations. Among these vectors, here we are concerned only with vector $\mathbf{Z} = u\mathbf{a}_1 + v\mathbf{a}_2$, which has the smallest components in both axial and circumferential directions [25]. Using simple geometric considerations, it follows that integers u and v must satisfy $l_2 u - l_1 v = d$ and $0 < t_1 v - t_2 u < N/d$. More useful, $\mathbf{Z}$ is decomposed along $\mathbf{T}$ and $\mathbf{C}_h$ as [25]:

$$N\mathbf{Z} = D\mathbf{C}_h + d\mathbf{T}, \tag{14}$$

where $D = t_1 v - t_2 u$. The infinitely-long CNT is alternatively described from the two-atom reduced cell bounded by the vectors $\mathbf{C}_h/d$ and $\mathbf{Z}$. For example, one can see from eq. (14) that N operations of $\mathbf{Z}$ extend over d translational cells. The rest of $(d-1)N$ carbon pairs of the d translational cells are filled by $d-1$ applications of $\mathbf{C}_h/d$.

Moving to the rolled-up geometry, a (l_1, l_2) CNT is described the "angular-helical" as an objective molecular structure with

$$\mathbf{X}_{n,\zeta_1,\zeta_2} = \mathbf{R}_2^{\zeta_2}\,\mathbf{R}_1^{\zeta_1}\mathbf{X}_n + \zeta_1\mathbf{T}_1, \quad j = 1, N_0. \tag{15}$$

The rotational matrix $\mathbf{R}_2$ corresponds to vector $\mathbf{C}_h/d$ and indicates an angular rotation of angle $\theta_2 = 2\pi/d$. Rotational matrix $\mathbf{R}_1$ of angle $\theta_1 = 2\pi D/N$ and the axial vector $\mathbf{T}_1 = d\mathbf{T}/N$ correspond to the screw vector $\mathbf{Z}$. Index n runs over the two atoms (the molecule) at locations $\mathbf{X}_j$ inside the reduced computational domain. Integers ζ_1 and ζ_2, with $-\infty < \zeta_1 < \infty$ and $0 \le \zeta_2 \le d-1$, label the various replicas of the initial domain.

We will accommodate this representation into the one-electron wavefunction solutions by representing them in terms of symmetry-adapted sums of localized orbitals, suitable for the helical and angular symmetry. We discuss next the steps that will be undertaken to enhance to symmetry-adapted modeling the current periodic boundary condition implementation in the computational package *Trocadero* [31]. We remind the reader that the microscopic model of interest is the nonorthogonal density functional theory-based tight binding model with two-center terms of Porezag et al. [32].

2.2.2 Symmetry-Adapted Tight Binding – Treatment of the Electronic Structure

Consider N_s the number of screw operations (typically ∞) over which the helical boundary condition is imposed and let N_a be the number of θ_2 rotations needed to fill the circumference of the quasi one-dimensional nanostructure. The symmetry-adapted Bloch sums write

$$|\alpha n, l\kappa\rangle = \frac{1}{\sqrt{N_a \cdot N_s}} \sum_{\zeta_1=0}^{N_s-1} \sum_{\zeta_2=0}^{N_a-1} e^{il\theta_2\zeta_2 + i\kappa\zeta_1} |\alpha n, \zeta_1\zeta_2\rangle, \tag{16}$$

where the Bloch factors are the eigenvalues of the commuting rotation and screw operators [27]. Here $l = 0, 1, ..., (N_a - 1)$ represents the angular number. To avoid the discomfort of introducing helical distances, $-\pi \leq \kappa < \pi$ represents the helical wavevector already normalized by the helical periodicity. As in Eq. (15), index n runs over the atoms located in the symmetry-adapted computational cell and $|\alpha n, \zeta_1\zeta_2\rangle$ refers to the orbital with symmetry α located on atom n, all in the symmetry-adapted cell indexed by ζ_1 and ζ_2. Lastly, to satisfy the generalized Bloch theorem, the $|\alpha n, \zeta_1\zeta_2\rangle$ orbitals are obtained by applying a $\mathbf{R}^{(\zeta_1,\zeta_2)}$ rotation to the orbitals $|\alpha n\rangle$ located in the (ζ_1, ζ_2) cell that are parallel with those situated in the initial $(0, 0)$ cell. Specifically, for the sp case:

$$\begin{pmatrix} |sn, \zeta_1\zeta_2\rangle \\ |p_x n, \zeta_1\zeta_2\rangle \\ |p_y n, \zeta_1\zeta_2\rangle \\ |p_z n, \zeta_1\zeta_2\rangle \end{pmatrix} = \begin{pmatrix} 1 & 0 & 0 & 0 \\ 0 & \cos(\zeta_1\theta_1 + \zeta_2\theta_2) & -\sin(\zeta_1\theta_1 + \zeta_2\theta_2) & 0 \\ 0 & \sin(\zeta_1\theta_1 + \zeta_2\theta_2) & \cos(\zeta_1\theta_1 + \zeta_2\theta_2) & 0 \\ 0 & 0 & 0 & 1 \end{pmatrix} \cdot \begin{pmatrix} |sn\rangle \\ |p_x n\rangle \\ |p_y n\rangle \\ |p_z n\rangle \end{pmatrix}. \tag{17}$$

Note that the s orbitals are not affected because of their intrinsic symmetry while the p_z ones are invariant as they are oriented along the long axis.

The symmetry-adapted Bloch elements between different angular and helical numbers of the Hamiltonian and overlap matrices vanish. Therefore, the eigenvalue problem for the atoms contained in the $N_s \cdot N_a$ symmetry-adapted domains becomes block-diagonal and it can be solved separately for each block labeled by l and κ:

$$\mathbf{H}(l\kappa) \cdot \mathbf{C}(j, l\kappa) = \varepsilon_j(l\kappa)\mathbf{S}(l\kappa) \cdot \mathbf{C}(j, l\kappa), \quad j = 1, ..., N. \tag{18}$$

The elements of eigenvector $\mathbf{C}$ represent the expansion coefficients in the basis (16) of the one-electron wavefunction solutions of the Schrödinger equation. Having [32] the elements of the Hamiltonian matrix – ε^0_α diagonal and $t^0_{\alpha',\alpha}$ off-diagonal – and of the overlap matrix $s^0_{\alpha',\alpha}$, the elements of $l\kappa$-dependent Hamiltonian $\mathbf{H}$ and overlap $\mathbf{S}$ matrices are:

$$\langle \alpha' n', l\kappa | H | \alpha n, l\kappa \rangle = \varepsilon^0_\alpha \delta_{nn'}\delta_{\alpha\alpha'} + \sum_{\zeta_2,\zeta_1} e^{-il\theta_2\zeta_2 - i\kappa\zeta_1} t_{\alpha'\alpha}(\mathbf{X}_{n',(\zeta_1,\zeta_2)} - \mathbf{X}_n), \tag{19}$$

$$\langle \alpha' n', l\kappa | \alpha n, l\kappa \rangle = \delta_{nn'}\delta_{\alpha\alpha'} + \sum_{\zeta_2,\zeta_1} e^{-il\theta_2\zeta_2 - i\kappa\zeta_1} s_{\alpha',\alpha}(\mathbf{X}_{n',(\zeta_1,\zeta_2)} - \mathbf{X}_n), \tag{20}$$

where

$$t_{\alpha'\alpha}(\mathbf{X}_{n',(\zeta_1,\zeta_2)} - \mathbf{X}_n) = \sum_{\alpha''=1}^{n_\alpha} t^0_{\alpha'',\alpha}(\mathbf{X}_{n',(\zeta_1,\zeta_2)} - \mathbf{X}_n) R^{(\zeta_1,\zeta_2)}_{\alpha',\alpha''}, \tag{21}$$

$$s_{\alpha',\alpha}(\mathbf{X}_{n',(\zeta_1,\zeta_2)} - \mathbf{X}_n) = \sum_{\alpha''=1}^{n_\alpha} s^0_{\alpha'',\alpha}(\mathbf{X}_{n',(\zeta_1,\zeta_2)} - \mathbf{X}_n) R^{(\zeta_1,\zeta_2)}_{\alpha',\alpha''}. \tag{22}$$

In comparison with the tight binding under periodic boundary conditions [24], in Eq. (18) we obtained a size reduction of the eigenvalue problem at the expense of carrying out diagonalizations at additional $l\kappa$ points. In view of the $O(N^3)$ computational time scaling, the advantage of the symmetry-adapted basis is evident.

2.2.3 Symmetry-Adapted Tight Binding Molecular Dynamics

The total electronic energy contained in the $N_s \cdot N_a$ symmetry-adapted domains writes:

$$E_{\text{band}} = 2 \sum_{j=1}^{n_\alpha N_0} \sum_{\kappa=-\delta\kappa(N_s-1)/2}^{\delta\kappa(N_s-1)/2} \sum_{l=0}^{N_a-1} f_j(l\kappa)\varepsilon_j(l\kappa), \tag{23}$$

where f is the Fermi function and $\delta\kappa = 2\pi/N_s$. Because E_{band} is invariant under the screw and angular rotations as well as under the permutations of atoms, the conditions for carrying out Symmetry-adapted MD from the tight binding potential are fulfilled. To perform MD, the forces acting on the N_0 atoms are needed. The force on the atom at $\mathbf{X}_m$ located due to the band energy, $\mathbf{F}_m = -\partial E_{\text{band}}/\partial \mathbf{X}_m$, writes:

$$\mathbf{F}_m = -2 \sum_{j,l\kappa} f_j(l\kappa) \left(\mathbf{C}^\dagger(j,l\kappa) \cdot \frac{\partial \mathbf{H}(l\kappa)}{\partial \mathbf{X}_m} \cdot \mathbf{C}(j,l\kappa) - \varepsilon_j(l\kappa)\mathbf{C}^\dagger(j,l\kappa) \cdot \frac{\partial \mathbf{S}(l\kappa)}{\partial \mathbf{X}_m} \cdot \mathbf{C}(j,l\kappa) \right), \tag{24}$$

which is the Hellmann-Feynman force. The above expressions are considered as $N_s \to \infty$ and κ becomes continuous. The derivatives of the Hamiltonian and overlap matrix elements are:

$$\frac{\partial \langle \alpha' n', l\kappa | H | \alpha m, l\kappa \rangle}{\partial \mathbf{X}_m} = \frac{1}{N_a N_s} \sum_{\zeta_2,\zeta_1} e^{-il\theta_2\zeta_2 - i\kappa\zeta_1} \sum_{\alpha''=1}^{n_\alpha} \frac{\partial t^0_{\alpha'',\alpha}(\mathbf{X}_{n',(\zeta_1,\zeta_2)} - \mathbf{X}_m)}{\partial \mathbf{X}_m} R^{(\zeta_1,\zeta_2)}_{\alpha',\alpha''}. \tag{25}$$

$$\frac{\partial \langle \alpha' n', l\kappa | \alpha m, l\kappa \rangle}{\partial \mathbf{X}_m} = \frac{1}{N_a N_s} \sum_{\zeta_2,\zeta_1} e^{-il\theta_2\zeta_2 - i\kappa\zeta_1} \sum_{\alpha''=1}^{n_\alpha} \frac{\partial s^0_{\alpha'',\alpha}(\mathbf{X}_{n',(\zeta_1,\zeta_2)} - \mathbf{X}_m)}{\partial \mathbf{X}_m} R^{(\zeta_1,\zeta_2)}_{\alpha',\alpha''}. \tag{26}$$

Derivatives $\partial t^0_{\alpha'',\alpha}/\partial \mathbf{X}_m$ and $\partial s^0_{\alpha'',\alpha}/\partial \mathbf{X}_m$ are given in [32]. We note that the two-body repulsive part of the tight binding potential [32] does not necessitate specific adjustments for symmetry-adapted molecular dynamics.

3 Applications of Symmetry-Adapted Modeling in Nanomechanics

3.1 Linear- and Nonlinear-Elastic Response of Carbon Nanotubes

3.1.1 Linear-Elastic Response

We now illustrate the applicability of the method in the linear-elastic deformation regime. One could carry out microscopic calculations of relaxed, elongated, and twisted carbon nanotubes described from a two-atom domain with Eq. (15) serving as the objective boundary conditions. The electronic states are modeled with the presented symmetry-adapted scheme coupled with the non-orthogonal two-centre tight binding model of carbon [32], implemented in the package Trocadero [31].

In order to define infinitesimal elastic moduli of a nanotube, we first identified the stress-free equilibrium geometries. We find that the structural parameter predictions given by the roll-up are adequate. The isometric mapping that wraps the graphene sheet into the cylindrical geometry is not precisely a nanotube at equilibrium as the carbon-carbon bond lengths will differ in general from their values in the flat geometry. We identified the equilibrium carbon nanotubes through conjugate gradient potential energy surface scans performed on the two-atom cell under different $|\mathbf{T}_1|$ values.

Figure 3a plots the obtained strain energy (W_0), defined as the energy (measured per atom) of the equilibrium CNT configuration measured with respect to the graphene, as a function of the CNT diameter ($2R$). The characteristic behavior $W_0 = C/2R^2$ is obtained with $C = 4.13\ \text{eVÅ}^2/atom$, in very good agreement with density functional theory data [35]. Note the large difference with the $2.2\ \text{eVÅ}^2/atom$ and $1.8\ \text{eVÅ}^2/atom$ values given by the first- and second-generation Brenner's potentials, respectively. No χ-dependence was obtained, as can be seen also from the insert showing W_0 versus χ for an equal-radius CNT family. Adopting a surface-without-thickness membrane [13] representation of graphene, the associated bending rigidity is $D_b = C/S_0$, where $S_0 = 2.6\ \text{Å}^2$ is the surface per atom defined by the CNT at equilibrium.

Axial strain (ε) to an (l_1, l_2) CNT was applied by changing $|\mathbf{T}_1|$ to $(1+\varepsilon)|\mathbf{T}_1|$, with ε in the $(-0.5{:}0.5\%)$ range. The intrinsic θ_1 and θ_2 angles were kept fixed. The obtained size dependence of $Y_s = (1/S_o)d^2W_0/d\varepsilon^2$ is displayed in Fig. 4b. In contrast with other results, Y_s appears insensitive to χ. The axial elasticity of carbon nanotubes appears similar to the in-plane one of graphene apart from effects due the tube curvature. Above $\sim$1.25 nm Y_s is practically constant and takes the 430 GPa nm value of graphene. The agreement with previous tight binding calculations [36], carried out in the translational representation of the carbon nanotubes, confirms the validity of our scheme. For $2R < 1.25$ nm Y_s softens, which is in disagreement for example with the data obtained using the second-generation Brenner's potential.

An axial twist rate (γ) was imposed by varying the intrinsic angle θ_1 to $\theta_1 + \gamma|\mathbf{T}_1|$. Because the symmetry-adapted tight binding scheme doesn't rely on translational symmetry, any γ can be prescribed. By contrast, limited γ choices are

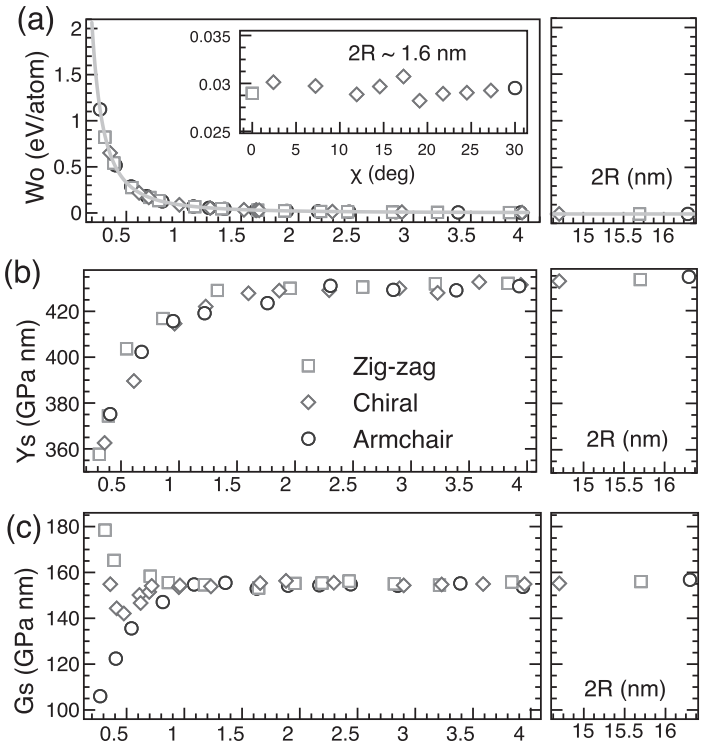

Fig. 3 (**a**) Curvature-strain energy W_0 (**b**) Young's Y_s and (**c**) shear modulus G_s as a function of the CNT diameter $2R$. Insert shows W_0 dependence with χ at a constant diameter

available in the translational formulation, making calculations cumbersome. The resulting shear strain $\varepsilon' = \gamma R$ was varied in the $(-0.5\%{:}0.5\%)$ range, while $|\mathbf{T}_1|$ was kept constant. Figure 4c displays the obtained surface shear modulus (G_s), defined as $G_s = (1/S_o)d^2W_0/d\varepsilon'^2$. For $2R > 1.25$ nm, G_s is not sensitive to χ and converges quickly to the 156 GPa nm value of graphene. This value is higher than the 113 GPa nm given by the second-generation Brenner's potential and is in excellent agreement with the 157 GPa nm from density functional theory. For $2R < 1.25$ nm there is a pronounced χ splitting with G_s bounded from above by zig-zag and from below by armchair carbon nanotubes.

The χ-dependence for G_s for $2R < 1.25$ nm unequivocally shows anisotropy. Interestingly, the HiPco-produced carbon nanotubes fall within this size-range. However, our tight binding data for $2R > 1.25$ nm shows that both Y_s and G_s are practically converged to the values of isotropic graphene. Thus, the isotropic CNT model is justified and we have $G_s = Y_s/2(1+\nu_s)$. The resulting Poisson ratio $\nu_s = 0.38$ is lower than the one obtained with the Brenner's potential [13] but still larger than in experiment. For practical reasons it is also useful to give a CNT elastic thin-shell model. Thus, we expressed $D_b = Yh^3/12$ and $Y_s = Yh$. Using our data we obtained $h = 0.8$ Å and $Y = 5.2$ TPa.

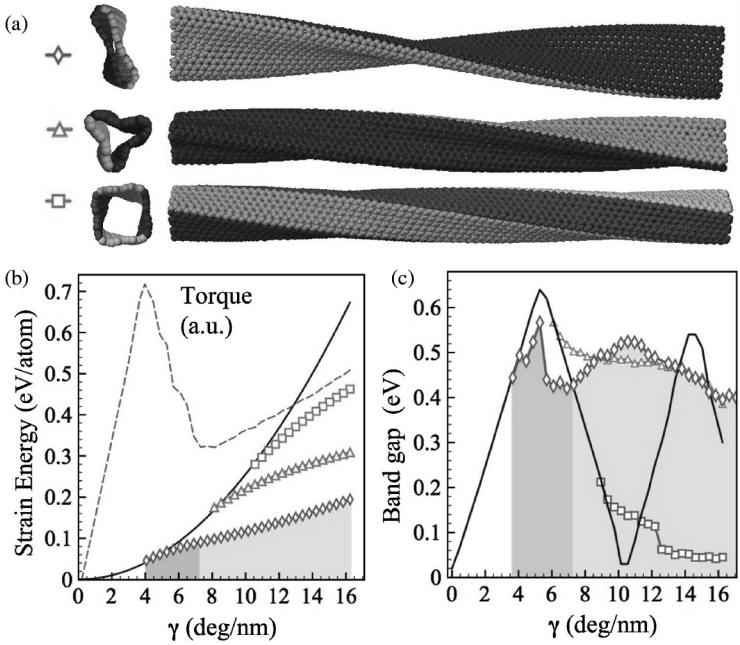

Fig. 4 (**a**) Rippling patterns in a (12,12) CNT under 10°/nm twist. Colors correspond to distinct azimuthal replicas of the objective domain. (**b**) Strain energy and (**c**) band gap vs. twist rate γ for cylinder and rippling modes. Torque (in arbitrary units) for the two-lobe mode is plotted in order to indicate the two stages of rippling, also marked with two gray levels

3.1.2 Nonlinear Elastic Response of Carbon Nanotubes in Torsion

Can the symmeyty-adapted modeling be useful beyond the linear elastic regime? We illustrate now the use of the method for studying torsional rippling deformations. Rippling represents a way of lowering energy by creating an inhomogeneous torsional strain coupled with the development of helicoidal ridges and furrows of positive and negative curvature, respectively. Due to the distributed nature, the long-range inter-wall interactions are also perturbed. For high fidelity modeling, accurate accounting of both covalent and van der Waals forces is needed. In principle, quantum mechanical calculations can provide both the morphological changes and the electronic behavior. There is ample evidence that an explicit quantum mechanica treatment of bonding gives an accurate description of carbon nanotube's mechanics. However, the usual translation-invariant formulation is computationally prohibitive for long-range elastic deformations with helical symmetry. To reduce the computational complexity, empirical classical potentials and continuum idealizations derived from classical potentials are widely used. When compared with quantum mechanical descriptions, these approaches are sometimes inaccurate, including for describing the linear elastic regime. Another obvious disadvantage is that the electronic response is not revealed.

We discuss single-wall carbon nanotubes in torsion under the constraint of constant length. Renouncing the translational symmetry allows to compute in an economical fashion the expected helical [13] rippling morphologies that characterize the initial stages of the nonlinear elastic response. For example, the wave-like modes for (12,12) CNT shown in Fig. 4a, were individually computed with objective MD from three objective cells delineated by the translational vector **T** but different θ_2 values, 180°, 120°, and 90°. Because these cells contain only 24, 18, and 12 atoms, respectively, the tight binding treatment can be comfortably applied. We studied in a decoupled way the rippling morphologies, unambiguously identify the fundamental (lowest-energy) mode, and pinpoint the level of twist beyond which the cylinder shape becomes first unstable, i.e., the bifurcation point.

The importance range of the various modes can be judged from Fig. 4b, which shows the computed strain-energies vs. γ. The curve obtained from a 4 atom objective cell with $\theta_2 = 30°$ (thin line) is a useful reference as the CNT's cylinder shape is preserved. At lower strains this state is stable but when strain exceeds 4°/nm the two-lobe rippling significantly lowers the elastic energy. The perfect structure can also assume the three- and four-lobe buckled states beyond 7°/nm and 9°/nm, respectively, but the two-lobe morphology stays favorable by a large margin. We conjecture that the various wave-like modes shown in Fig. 4a exist as distinct metastable states and twisting doesn't mix them by driving further circumferential rippling.

The evolution of torque (energy derivative with γ), Fig. 4b, further reveals that the two-lobe rippling develops in two stages. The first is a *transient* one and initiates at the bifurcation, where the linear torque variation is interrupted by a rather abrupt drop. The cylinder shape develops ridges and furrows as the torque's rate of change is negative. The minimum distance between furrows decreases until a van der Waals equilibrium distance of 3.4 Å is reached at 7.2°/nm. Here the transient stage is complete and torque's rate of growth switches from negative to positive. In this second stage there is no notable change in shape of the collapsed cross section.

Figure 4c shows the variations in the electronic band gap for the idealized cylinder and rippling modes. Band-gap information is important because of the relationship with the experimentally-relevant CNT resistance. For the idealized case, the band gap is periodically modulated. During one period $\Delta\gamma$, it grows in a linear fashion, reaches a maximum at halfway, then decreases to zero. These features are in agreement with predictions of Yang and Han [37] developed from the band structure of graphene: uniformly twisted carbon nanotubes are metallic only when the metallic wavefunction of graphene is commensurated with the CNT's circumference. Otherwise, they are semiconducting. Due to the linearity of the dispersion relation of graphene near its Fermi level, band gap varies in a linear fashion with a $3t_0R$ slope. R is the CNT's radius and t_0 is the tight binding hopping element. It also follows [37] that $\Delta\gamma = d_{C-C}/R^2$, where d_{C-C} is the C–C bond length. Fitting to our data gives $t_0 = 2.72$ eV and $d_{C-C} = 1.42$ Å, in agreement with the actual values of these parameters.

The generality of the above behavior is demonstrated in Fig. 5, summarizing results from a series of similar calculations performed on armchair carbon

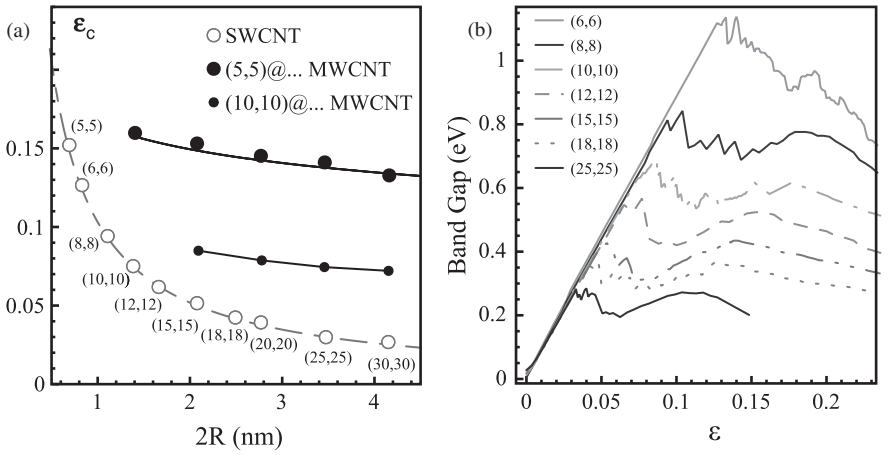

Fig. 5 (**a**) Critical shear strain vs. CNT's diameter for SW (*open circles*) and MW (*full circles*) armchair carbon nanotubes. (**b**) Changes in the band gap with the shear strain for armchair SWcarbon nanotubes

nanotubes. During torsion the ideal CNT wall experiences a shear strain $\varepsilon = \gamma R$. Figure 5a plots the obtained critical shear ε_c, which exhibits a scaling $\varepsilon_c = 0.1([nm]/2R)^{0.99}$. Figure 5b reveals the band gap dependence with ε. In agreement with the idealized model, the linear regime data collapses onto a common line with a $3t_0$ slope. However, beyond ε_c, the idealized model based on the homogeneous strain assumption cannot be used.

3.2 Stability of Polycrystalline and Hexagonal Si Nanowires

In spite of a large body of experimental [38–40] and theoretical [41–49] research, the ground state of quasi one-dimensional silicon structure at the lowest diameters is not yet known. Relying on thermodynamic arguments, one conjectures that in relatively thick nanowires the influence of surfaces is less important and arrangements with bulklike cores are more likely. However, as the diameter is decreased, surfaces are becoming increasingly important in the nanowire energetic balance [45], and quasi one-dimensional organizations with non-cubic core structures but low surface energies are possible.

To describe the ground state Si nanowire structure at sizes of below 10 nm, several candidates have been already envisioned: It was predicted [45] that an enhanced stability can be obtained in polycrystalline achiral Si nanowires constructed with five identical crystalline prisms exposing only low energy (001) Si surfaces. In another recent study [46], hexagonal nanowires with hexagonal cross sections were found to be the most stable. Note that although nanowires with hexagonal cores are prevalent in III-V zinc-blende semiconductors [50], they have been synthesized also in Si [40]. Finally, icosahedral Si quantum dots [51, 52] constructed

from tetrahedral blocks were proposed. Because of the low formation energy of the exposed (111) surfaces, these dots are very stable. One-dimensional nanowires assembled from icosahedral dots appeared [48] more favorable than the achiral pentagonal nanowires of [45].

3.2.1 Structures of Polycrystalline and Hexagonal Si Nanowires

We now discus the structure of the three nanowire motifs presented in Figs. 6 and 7. Although all three motifs have translational symmetry, they can be more economically described in the "angular-helical" representation discussed earlier.

Table 1 summarizes the exact values of the domain parameters θ_1 and θ_2 as well as algebraic expressions for the number of atoms N_0 and the number of surface atoms N_{sf} in the Symmetry-adapted domain as a function of the number of atomic layers L. The precise T_1 value is model dependent and will be determined by simulations.

The nanowire shown in Fig. 6a, labeled P, exhibits a five-fold rotational symmetry. The exposed five equivalent (001) surfaces have dimer rows oriented parallel with respect to the nanowire axis. At the center of this nanowire there is a channel of pentagonal rings. The symmetry-adapted computational domain shown in blue (dark gray) is a triangular prism limited by two (111) and one (001) surfaces. The associated angular parameters are $\theta_1 = 0$ and $\theta_2 = 2\pi/5$ while T_1 equals the periodic boundary condition periodicity T. Thus, in comparison with the traditional periodic boundary condition scheme, symmetry-adapted molecular dynamics reduces to $1/5$ the number of atoms that need to be accounted for. Note that to form the nanowire, the (111) surfaces of the symmetry-adapted domains are connected through low energy stacking fault defects. Because in the bulk Si the two (111) planes of the

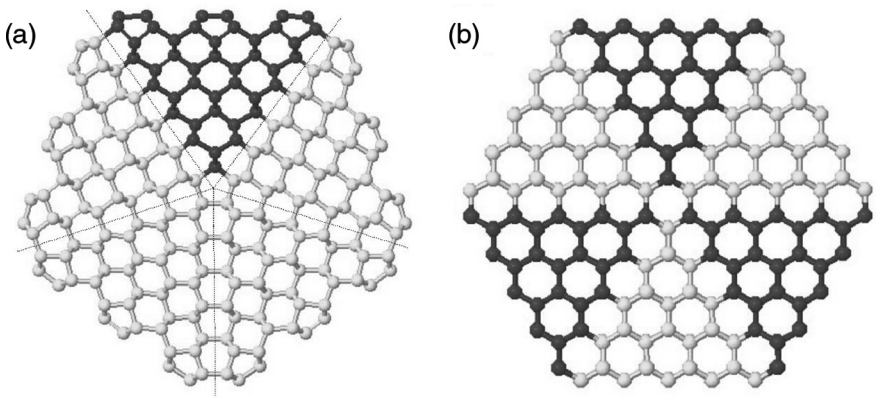

Fig. 6 (**a**) Pentagonal Si nanowire (labeled P). Surface is shown in a reconstruction with *symmetric* dimers, as described with a Tersoff potential. *Dotted lines* indicate the stacking fault planes. The computational "angular-helical" domains are shown in blue atoms. (**b**) Hexagonal Si nanowire (labeled H) with hexagonal cross section. The surface is shown as unrelaxed. Domains with same ζ_1 are shown in same color. For both nanowires only axial views are shown

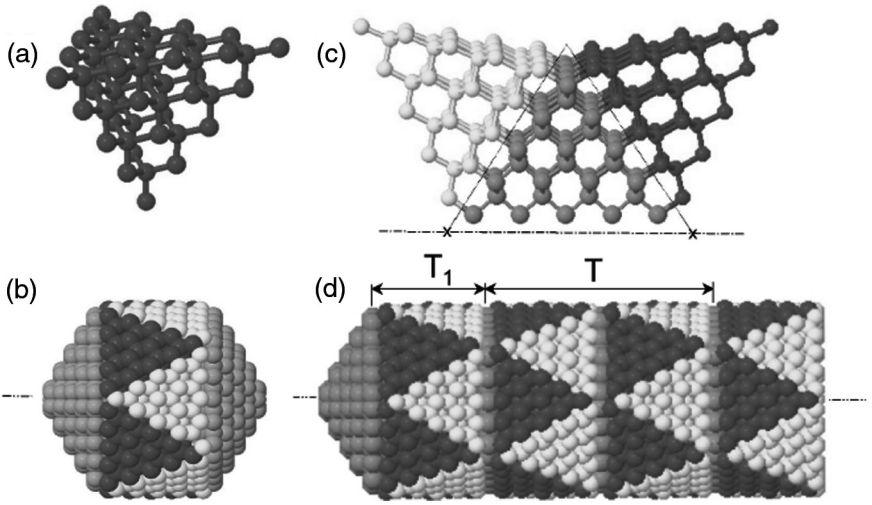

Fig. 7 (**a**) A tetrahedron building block truncated from the bulk Si exposes four (111) surfaces. (**b**) Icosahedral Si dot composed of twenty equivalent tetrahedron building blocks. With a domain composed of three tetrahedron blocks, shown in (**c**), a nanowire (labeled I) with pentagonal cross section, shown in (**d**), can be constructed based on formula describing the nanowire in the "angular-helical" and parameters entered in Table 1 corresponding to $L = 5$. Alternatively, the I nanowire can be constructed from aligned icosahedral Si dots sharing the tetrahedron building blocks shown in gray

Table 1 Comparison of the symmetry-adapted cells for the P, H, and I nanowires. L is the number of layers, N_0 is the total number of atoms, and N_{sf} is the number of surface atoms

Nanowire	P	H	I
θ_1	0	$\pi/3$	$\pi/5$
θ_2	$2\pi/5$	$2\pi/3$	$2\pi/5$
N_0	$2(L-1)(2L-1)$	$2L^2$	$0.5L(L+1)(2L+1)$
N_{sf}	$2(L-1)$	$2L$	$L(L+1)$

triangular prism form an angle $\theta = 2\tan^{-1}(1/\sqrt{2})$, which is slightly different from θ_2, each domain stores elastic energy corresponding to a shear deformation with $\varepsilon = \theta_2 - \theta$.

Figure 6b shows the structure of a nanowire motif with a hexagonal cross section, but three-fold rotational symmetry. This nanowire, labeled H, has a hexagonal core structure. Although its surfaces are equivalent, they are shifted in an alternating manner along the nanowire axis by half of the translational period T. The symmetry-adapted computational domain represents 1/6 of the translational domain. Its parameters are $\theta_1 = \pi/3$, $T_1 = 0.5T$, and $\theta_2 = 2\pi/3$. The non-zero value of θ_1 indicates that the H nanowires is generated by repeated screw and pure rotations.

The last nanowire motif considered, labeled I, also exhibits a five-fold rotational symmetry. The tetrahedron block shown in Fig. 7a is truncated directly from the

bulk. It exposes only low-energy (111) surfaces and all faces are equilateral triangles. Twenty such blocks are combined through low-energy stacking faults to form the dot shown in Fig. 7b, having icosahedral I_h symmetry. The combination of three blocks shown in Fig. 7c represents the symmetry-adapted domain for the I nanowire shown in Fig. 7d. The associated angular parameters are $\theta_1 = \pi/5$, $\theta_2 = 2\pi/5$. Thus, with Eq. (15) this nanowire is built from screw and pure rotation isometries.

In the I nanowire one can identify two types of blocks: blocks (shown with yellow/light gray and blue/dark gray) that, like in the I_h dot, expose one facet and blocks (shown in gray) in which all facets are in contact with other blocks. As discussed before [48], the I nanowire can be also thought of as being composed of aligned polycrystalline I_h Si quantum dots that share the tetrahedron blocks shown in gray (i.e., five tetrahedral blocks at each interface). In this respect, the two crosses separated by a distance T_1 in Fig. 7c mark the centers of two virtual I_h dots sharing the gray blocks. This picture helps to comprehend the strain accumulated in the I nanowire, discussed next.

As in the case of the P nanowires, the mismatch resulted when combining the bulk tetrahedron blocks to form the I_h dot and the I nanowire introduces strain. In the high symmetry of the I_h dot the 20 tetrahedron blocks are equivalent and thus the mismatch strain will be equally distributed among them. More specifically, since at each vortex a radial channel of pentagonal rings is formed, each tetrahedron block around it accumulates elastic shear energy corresponding to a strain $\varepsilon = \theta_2 - \theta$. As each tetrahedron is delimited by three radial channels, it follows that the exposed faces are equilateral triangles, as can be also noted from Fig. 7b. The symmetry lowering to the I nanowire superposes additional elastic energy. In an icosahedron the tetrahedron building blocks are not regular (i.e., the exposed faces are equilateral while the internal ones are isosceles triangles). Thus, the (110) planes of the gray blocks of Fig. 7b (to be shared in the I nanowire construction) are not perpendicular on the nanowire long axis. Consequently, the internal blocks will undergo additional elastic deformation, specifically by decreasing the angle made by the two (111) facets that join into the circumferential edge, Fig. 7b, such that the middle transversal (110) plane becomes perpendicular to the nanowire axis. The other tetrahedron type will also be affected by this adjustment and the exposed faces will become isosceles triangles in the one-dimensional structure. From this qualitative picture one can immediately conjecture that the I nanowires will store a larger strain than the P nanowires and the I_h dots.

We finally note that in the I nanowires the periodic boundary condition treatment is unnatural as T is L-dependent and the number of atoms in the cell under periodic boundary condition increases significantly (as $\sim L^3$). For example, for $L = 6$ there are 2730 Si atoms in the cell under periodic boundary condition but only 273 atoms in the symmetry-adapted one.

3.2.2 Structural Optimizations

Which non-bulk nanowire structural motif is in fact more energetically favorable and therefore more likely to be stable? To answer this question we recognize that

the accuracy of any microscopic investigation depends critically on the level of theory behind the description of the Si-Si interatomic interactions. Unfortunately, accurate *ab initio* methods formulated in the typical periodical boundary conditions context are computationally demanding and studies employing these methods can be carried out only at the smallest diameters [42, 44, 47]. They are used to complement larger scale microscopic calculations based on empirical classical potentials [53, 54], which are typically assumed to be less accurate only in the smallest size range due to the enhanced role of surfaces.

Consider for instance the description of the surface reconstruction as obtained with the widely used Stillinger-Weber [53] and Tersoff [54] classical potentials, both used in [45, 46, 48] to describe the pentagonal nanowire that exposes (001) facets. The (001) Si surface has been studied with these potentials [55] and a p(2×1) *symmetric* dimer pattern was found to be the most stable. However, with density-functional theory it was found that the *alternating* asymmetric buckling of surface dimers p(2×2) is more favorable. Since the *asymmetric* buckling is not captured, the classical treatment [53, 54] for the thinnest nanowires exposing (001) surfaces will not be accurate.

We performed the structural optimization on the three selected nanowires by the proposed symmetry-adapted tight binding molecular dynamics method, carried out with a 1 fs time step, followed by conjugate gradient energy minimization scans for several T_1 parameter values until the optimal configuration was identified. Computations were carried out on the fundamental domains addressed in Table 1 for all I nanowires and for the H nanowires with odd L. Larger domains, with $2T_1$ for the P nanowires and $2\theta_2$ for the H nanowires with even L, were also used in order to describe the alternating reconstructions of the surfaces. Exploiting symmetry has the potential danger of missing minima with lower symmetry. Our additional calculations under periodic boundary condition carried out for the smallest nanowires (with $L = 2$) showed agreement with the symmetry-adapted data.

Figure 8a presents the optimal surface reconstruction for two P nanowire domains, showing an alternating buckled dimer reconstruction on top. Accounting correctly for the surface reconstruction appeared important especially for the thinnest nanowires where the surface to volume ratio is largest. For example, we obtained a 20 meV/atom energy lowering from the non-alternating buckled to the alternating buckled pattern for the P nanowire with $L = 2$.

The H nanowire surface exposes dimer rows aligned perpendicularly on the nanowire axis. Our symmetry-adapted tight binding molecular dynamics optimization procedure obtained again an alternating buckled pattern of the surface dimers, as presented in Figure 8b. This appears in disagreement with our obtained classical description which does not account for the buckling effect. Regarding the surfaces of the I nanowires, we noted that the characteristic surface buckling of the (111) surface was severely reduced with the increase in diameter. In fact, above $2R = 2.5$ nm the surface was practically built up from flat hexagonal rings. The alternating buckled pattern was obtained on the edge surface dimer rows formed at the interface between tetrahedrons. By contrast, the surface did not appear flattened and the edge dimers did not buckle in the classical treatment.

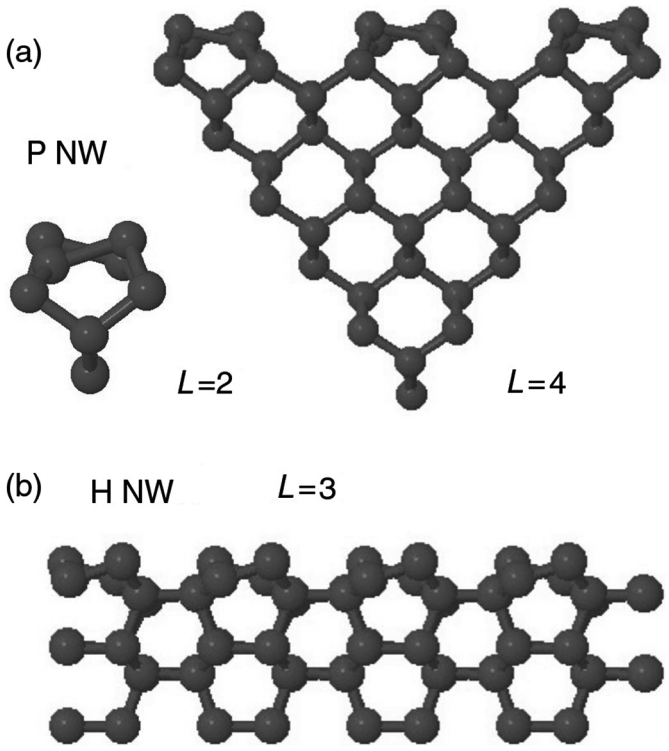

Fig. 8 (**a**) Symmetry-adapted domain (axial view) for the P nanowires with $L = 2$ and $L = 4$. The alternating buckled dimer reconstruction pattern of the surface can be observed. (**b**) Side view of the symmetry-adapted domain for the H nanowires with $L = 3$ of length $4T_1$, showing on top the buckled dimer alternating pattern

In Figure 9 we report the obtained stability data for the three nanowire motifs as described by the two microscopic models. As can be seen from Figure 9a, which plots the nanowires formation energies E (measured with respect to atomic energy values) in the tight binding model as a function of diameter $2R$, the P and H nanowire motifs emerge as the most favorable. (Practically the two curves are overlapping at diameters above 2 nm.) Surprisingly, the I nanowire is favorable only at the very small diameters, below $\sim$2.5 nm, when the I curve intersects the P one. Above this value, this nanowire becomes unfavorable. Interestingly, Figure 9b shows that a very different conclusion can be obtained if one relies on the classical potential data. The formation energy curves for the three nanowires are very close together. In agreement with previous investigations [48], the I wire appears now more favorable than the P one and the intersections between the I and P curves, marked by the down arrow, is delayed until $\sim$9 nm. In agreement also with the previous comparison [46] based on the classical Stillinger-Weber potential, the H nanowire motif appears overall more favorable than the P one. Comparing now the I and H nanowires, we see that below 6 nm in diameter the I nanowire is favored.

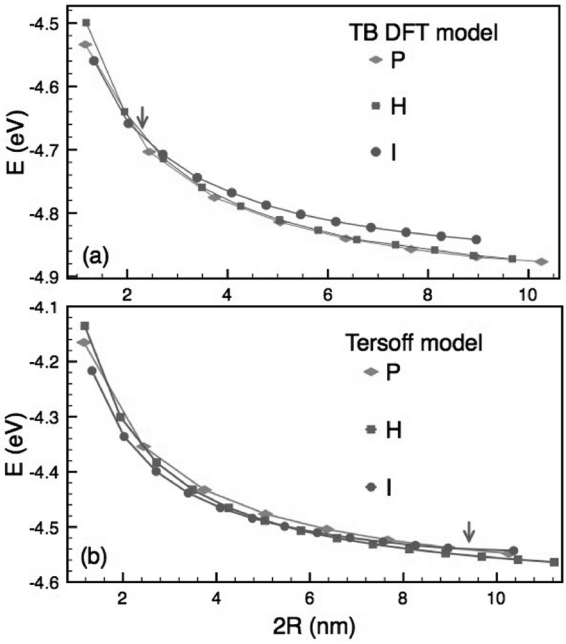

Fig. 9 Size dependence of the cohesive energy for the P, H, and I Si nanowires. The (**a**) density functional theory-based tight binding potential and (**b**) classical Tersoff potential give different energetic orderings. Arrows mark intersections of I and P energy curves

3.2.3 Comparison of the Tight Binding and Classical Potential Simulation Results

To rationalize the differences between Fig. 9a, b we have analyzed in more detail how the two microscopic models are describing each nanowire motif. Figure 10a,b,c plots over a large diameter range the obtained $E - E_{\text{bulk}}$ values for all nanowires as obtained with the tight binding and Tersoff atomistic descriptions. We found it instructive to perform a Wulff decomposition of the obtained cohesive energy data as:

$$E - E_{\text{bulk}} = \delta E_{\text{bulk}} + E_{\text{sf}} + E_{\text{e}}, \tag{27}$$

where E_{bulk} represents the cohesive energy of the crystalline nanowire bulk, i.e., cubic diamond bulk (-4.953 eV and -4.628 eV for tight binding and Tersoff potential, respectively) for the P and I nanowires and the hexagonal bulk Si (-4.943 eV and -4.625 eV for the tight binding and Tersoff potential, respectively) for the H nanowire. In Eq. (13) δE_{bulk} is the bulk energy correction, which captures the elastic strain stored in the nanowire core. The surface E_{sf} and edge E_{e} energies have analytic expressions constructed by taking into account the structural parameters of the nanowires. A Wulff decomposition extrapolation approach was used before to predict formation energies of nanowires at larger sizes [45]. Here, by identifying in the atomistic data the magnitude of the various contributions, we use it to obtain more insight about the differences between the two models.

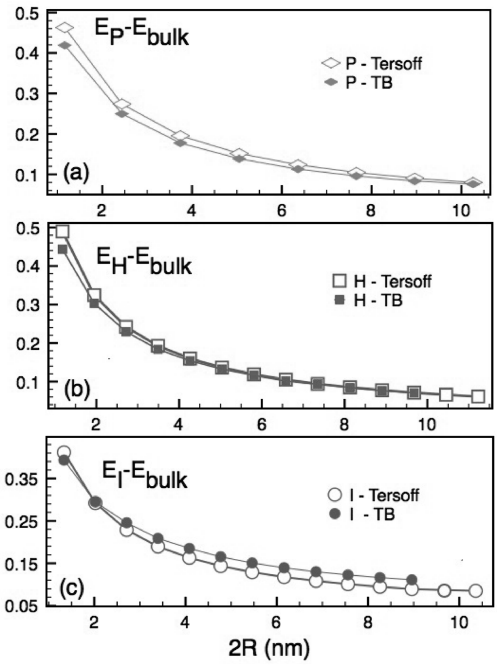

Fig. 10 (**a**) P, (**b**) H, and (**c**) I Si nanowires described with the tight binding (*full markers*) and Tersoff (*open markers*) potential. The zero of energy is taken to be the cohesive energy of the cubic diamond Si in (**a**) and (**c**), and the hexagonal Si in (**b**). The energy is measured in eV per atom

In Fig. 10a we see that overall the tight binding description of the P nanowire gives a lower energy. The differences are especially significant at the smaller sizes (44 meV at $L = 2$) and they diminish as the nanowire diameter is increased. Using the structural information entered in Table 1 and recognizing that this nanowire structure has no edge energy penalty, we obtain that the cohesive energy should scale with the number of layers L as

$$E_P(L) - E^c_{\text{bulk}} = \delta E_{\text{bulk}} + \frac{\gamma_P}{2L-1}, \tag{28}$$

where γ_P is the surface energy penalty per surface atom and δE_{bulk} represents the shear elastic energy stored in these structures. Fitting to the atomistic data we obtained γ_P of 1.25 eV/atom with tight binding and 1.39 eV/atom with Tersoff description. For both models we found that δE_{bulk} is small and can be neglected. Thus, the energetic differences noted in Fig. 10a can be attributed mainly to the inability of the Tersoff potential to correctly describe the exposed Si (001) surfaces.

Moving on to the H nanowire, Fig. 10b shows similar differences with a classical–tight binding agreement at large diameters. The H nanowire does not contain edge and bulk correction terms. Relying on the algebraic form

$$E_H(L) - E^w_{\text{bulk}} = \frac{\gamma_H}{L}, \tag{29}$$

a least-squares fitting of the two data sets obtained γ_H as 0.88 eV/atom in tight binding and 0.97 eV/atom with the classical potential.

Figure 10c shows even larger differences between the two I nanowire descriptions. While at the lowest diameter the tight binding model yields a lower energy, the classical potential-based modeling gives a lower energy for $L \geq 4$ or $2R \geq 2.5$ nm. We fitted the data to the algebraic form

$$E_I(L) - E^c_{\text{bulk}} = \delta E_{\text{bulk}} + \frac{\gamma_I}{L + 0.5} + \frac{12\delta}{(L+1)(2L+1)}, \tag{30}$$

which was constructed based on the structural parameters entered in Table 1 and the observation that there are $6L$ edge atoms in each computational domain. Due to the different surface reconstruction above 2.5 nm in diameter, the first two tight binding data points were not included in the fitting. For δE_{bulk} we obtained 36 meV/atom with tight binding versus 21 meV/atom with classical. Both models confirm the I nanowire stores significant strain energy but due to the errors in reproducing the elastic constants, the strain component is not well represented by the classical model. Further, we found the flattened surface obtained with tight binding has a higher 980 meV/atom cost when compared with the 900 meV/atom obtained classically. Finally, we found that the buckling of the dimers located on the edges lowers the tight binding energy as $\delta = -37$ meV/atom. A δ value of 38 meV/atom obtained from the classical data agrees with our observation that this model does not capture the dimer buckling. As can be seen from Eq. (30), the edge energy component is the least important, and the tight binding description gives a higher energy because the bulk correction and the surface energy count more in the energy balance. We have summarized all the fitted data of the energy components in the Wulff decomposition in Table 2.

Table 2 Summary of energy values obtained from the Wulff-like energy decomposition of the three nanowires

Nanowire		P	H	I
E_{bulk}(eV)	Tight binding	−4.953	−4.943	−4.953
	Tersoff	−4.628	−4.625	−4.628
δE_{bulk}(meV)	Tight binding	0	–	36
	Tersoff	0	–	21
γ (eV)	Tight binding	1.25	0.88	0.98
	Tersoff	1.39	0.97	0.90
δ (meV)	Tight binding	–	–	−37
	Tersoff	–	–	38

4 Conclusion

In conclusion, symmetry adapted tight binding modeling is a versatile and efficient computational technique for nanomechanics. Based on the obtained modeling results, one has the possibility to next construct a continuum, computational efficient model of the nano objects that can be used in engineering applications. Here we proved the abilities of this method to uncover the linear and nonlinear elastic response of carbon nanotubes from a density-functional-based tight binding modeling of the covalent bond. The critical strain beyond which nanotubes behave nonlinearly in torsion, the most favorable rippling morphology, and the twist- and morphology-related changes in fundamental band gap were identified from a rigorous atomistic description.

From the presented investigations on the stability of Si nanowires we see that the use of a quantum-mechanical description of the atomic bonding is critical as the classical potentials [54] introduces significant errors. Moreover, these errors are not systematic: On one hand, for the P and H nanowires the errors are larger at smaller diameters as they are mainly caused by the inability of the classical potential to describe the surface reconstruction. On the other hand, for the I nanowire the errors are large even at large diameters, as they are due to the inability to describe the strain stored in the nanowire core as well as the higher surface energy penalty. The magnitude of these errors are causing the energetic ordering of the nanowire structures not to be identical in the two microscopic descriptions. Hence, different stability conclusions [46, 48] can be reached from the two data sets. We note that the usual approach [45, 46] of complementing the large scale classical calculations with expensive quantum calculations carried out at the smallest diameters (i.e., that assumes that corrections are needed at the smallest diameters only) should be used with care. For example, judging the I nanowire stability by combining the Tersoff data with the affordable first two tight binding data points under periodic boundary condition would be deceiving.

Acknowledgements TD acknowledges NSF CAREER CMMI-0747684 for supporting this research.

References

1. S. Iijima, Helical microtubules of graphitic carbon. Nature, **354** (6348), 56–58 (1991)
2. N.G. Chopra, R.J. Luyken, K. Cherrey, V.H. Crespi, M.L. Cohen, S.G. Louie, A. Zettl, Boron nitride nanotubes. Science, **269** (5226), 966–967 (1995)
3. H. Dai, E.W. Wong, Y.Z. Lu, S. Fan, C.M. Lieber, Synthesis and characterization of carbide nanorods. Nature, **375** (6534), 769–772 (1995)
4. P. Yang, C.M. Lieber, Nanorod-superconductor composites: a pathway to materials with high critical current densities. Science, **273** (5283), 1836–1840 (1996)

5. D. Qian, G.J. Wagner, W.K. Liu, A multiscale projection method for the analysis of carbon nanotubes. Comput. Method Appl. Mechan. Eng. **193** (17–20), 1603–1632 (2004)
6. T. Belytschko, S.P. Xiao, G.C. Schatz, R.S. Ruoff, Atomistic simulations of nanotube fracture. Phys. Rev. B, **65** (23), 235430 (2002)
7. B.I. Yakobson, C.J. Brabec, J. Bernholc, Nanomechanics of carbon tubes: instabilities beyond linear response. Phys. Rev. Lett. **76** (14), 2511–2514 (1996)
8. K.M. Liew, C.H. Wong, X.Q. He, M.J. Tan, S.A. Meguid, Nanomechanics of single and multiwalled carbon nanotubes. Phys. Rev. *B*, **69** (11), 115429 (2004)
9. X. Li, W. Yang, B. Liu, Bending induced rippling and twisting of multiwalled carbon Nanotubes. Phys. Rev. Lett., **98** (20), 205502 (2007)
10. W.K. Liu, E.G. Karpov, S. Zhang, H.S. Park, An introduction to computational nanomechanics and materials. Comput. Meths Appl. Mechan. Eng. **193** (17–20), 1529–1578 (2004)
11. W.W. Gerberich, W.M. Mook, C.R. Perrey, C.B. Carter, M.I. Baskes, R. Mukherjee, A. Gidwani, J. Heberlein, P.H. McMurry, S.L. Girshick, Superhard silicon nanospheres. J. Mechan. Phys. Solids, **51** (6), 979–992 (2003)
12. M. Arroyo, T. Belytschko. An atomistic-based finite deformation membrane for single layer crystalline films. J. Mechan. Phys. Solids, **50** (9), 1941–1977 (2002)
13. M. Arroyo, T. Belytschko, Nonlinear mechanical response and rippling of thick multiwalled carbon nanotubes. Phys. Rev. Lett. **91** (21), 215505 (2003)
14. S. Zhang, S.L. Mielke, R. Khare, D. Troya, R.S. Ruoff, G.C. Schatz, T. Belytschko, Mechanics of defects in carbon nanotubes: atomistic and multiscale simulations. Phys. Rev. *B*, **71** (11), 115403 (2005)
15. A.Y.T. Leung, X. Guo, X.Q. He, H. Jiang, Y. Huang, Postbuckling of carbon nanotubes by atomic-scale finite element. J. Appl. Phys., **99**, 124308 (2006)
16. B. Liu, H. Jiang, Y. Huang, S. Qu, M.F. Yu, K.C. Hwang, Atomic-scale finite element method in multiscale computation with applications to carbon nanotubes. Phys. Rev. *B*, **72** (3), 35435 (2005)
17. P. Zhang, Y. Huang, P.H. Geubelle, P.A. Klein, K.C. Hwang, The elastic modulus of single-wall carbon nanotubes: a continuum analysis incorporating interatomic potentials. Int J Solids Struct., **39** (13–14), 3893–3906 (2002)
18. P. Zhang, H. Jiang, Y. Huang, P.H. Geubelle, K.C. Hwang, An atomistic-based continuum theory for carbon nanotubes: analysis of fracture nucleation. J. Mechan. Phys. Solids, **52** (5), 977–998 (2004)
19. L.V. Zhigilei, C. Wei, D. Srivastava, Mesoscopic model for dynamic simulations of carbon nanotubes. Phys. Rev. *B*, **71** (16), 165417 (2005)
20. R.M. Martin, Electronic structure: basic theory and practical methods. (*Cambridge University Press*, Cambridge, UK, 2005)
21. N.M. Ghoniem, E.P. Busso, N. Kioussis, H. Huang, Multiscale modelling of nanomechanics and micromechanics: an overview. Philos. Mag., **83** (31), 3475–3528 (2003)
22. W. Kohn, L.J. Sham, Self-consistent equations including exchange and correlation effects. Phys. Rev., **140** (4A), A1133–A1138 (1965)
23. J.C. Slater, G.F. Koster, Simplified LCAO method for the periodic potential problem. *Phys. Rev.*, 94 (6), 1498–1524 (1965)
24. C.M. Goringe, D.R. Bowler, E. Hernández, Tight binding modelling of materials. Rep Prog Phys. **60** (12), 1447–1512 (1997)
25. R. Saito, G. Dresselhaus, M.S. Dresselhaus, Physical properties of carbon nanotubes. (Imperial College Press, London, 2005)
26. P.B. Allen, Nanocrystalline Nanowires: III. Electrons. Nano Lett, **7** (5), 1220–1223 (2007)
27. V.N. Popov, An equivalent non-orthogonal tight binding formalism using Bloch sums adapted for screw and translation operations can be found in . *New J. Phys.*, **6** (1), 17 (2004)
28. C.T. White, D.H. Robertson, J.W. Mintmire, Helical and rotational symmetries of nanoscale graphitic tubules. Phys. Rev. *B*, **47** (9), 5485–5488 (1993)
29. R.D. James, Objective structures. J. Mechan. Phys. Solids, **54**: 2354–2390 (2007)
30. T. Dumitrică, R.D. James, Objective molecular dynamics. J. Mechan. Phys. Solids, **55** (10), 2206–2236 (2007)

31. R. Rurali, E. Hernández, Trocadero: a multiple-algorithm multiple-model atomistic simulation program. Comput. Mater. Sci., **28** (2), 85–106 (2003)
32. D. Porezag, T. Frauenheim, T. Köhler, G. Seifert, R. Kaschner, Construction of tight binding-like potentials on the basis of density-functional theory: application to carbon. Phys. Rev. *B*, **51** (19), 12947–12957 (1995)
33. C.H. Xu, C.Z. Wang, C.T. Chan, K.M. Ho, A transferable tight binding potential for carbon. *J. Phys.:* Condens. Matt., **4**, 6047–6054 (1992)
34. M. Born, G. R. Oppenheimer. Zur Quantentheorie der Molekeln. Ann. Physik, **84**, 457 (1927)
35. K.N. Kudin, G.E. Scuseria, B.I. Yakobson, C_2, F, BN, and C nanoshell elasticity from ab initio computations. Phys. Rev. *B*, **64** (23), 235406 (2001)
36. E. Hernández, C. Goze, P. Bernier, A. Rubio, Elastic properties of C and $B_xC_yN_z$ composite nanotubes. Phys. Rev. Lett., **80** (20), 4502–4505 (1998)
37. L. Yang, J. Han, Electronic structure of deformed carbon nanotubes. Phys. Rev. Lett., **85** (1), 154 (2000)
38. Y. Wu, Y. Cui, L. Huynh, C.J. Barrelet, D.C. Bell, C.M. Lieber, Controlled growth and structures of molecular-scale silicon nanowires. Nano Lett, **4** (3), 433–436 (2004)
39. M. Takeguchi, M. Tanaka, H. Yasuda, K. Furuya, Real-time high-resolution transmission electron microscopy observation of the growth process of (001) surfaces on a nanometer-sized Si multiply twinned particle. Surf Sci, **493** (1), 414–419 (2001)
40. A.F. Morral, J. Arbiol, J.D. Prades, A. Cirera, J.R. Morante, Synthesis of silicon nanowires with wurtzite crystalline structure by using standard chemical vapor deposition. Adv. Mater, **19**, 1347–1351 (2007)
41. J. Bai, X.C. Zeng, H. Tanaka, J.Y. Zeng, Metallic single-walled silicon nanotubes. Proc Nat Acad Sci., **101** (9), 2664–2668 (2004)
42. T. Dumitrică, M. Hua, B.I. Yakobson, Endohedral silicon nanotubes as thinnest silicide wires. Phys. Rev. *B*, **70** (24), 241303 (2004)
43. R. Rurali, N. Lorente, Metallic and semimetallic silicon $< 100 >$ nanowires. Phys. Rev. Lett., **94** (2), 26805 (2005)
44. R. Kagimura, R.W. Nunes, H. Chacham, Structures of si and ge nanowires in the subnanometer range. Phys. Rev. Lett., **95** (11), 115502 (2005)
45. Y. Zhao, B.I. Yakobson, What is the ground-state structure of the thinnest si nanowires? Phys. Rev. Lett., **91** (3), 35501 (2003)
46. I. Ponomareva, M. Menon, D. Srivastava, A.N. Andriotis, Structure, stability, and quantum conductivity of small diameter silicon nanowires. Phys. Rev. Lett., **95** (26), 265502 (2005)
47. I. Ponomareva, M. Menon, E. Richter, A.N. Andriotis, Structural stability, electronic properties, and quantum conductivity of small-diameter silicon nanowires. Phys. Rev. *B*, **74** (12), 125311 (2006)
48. K. Nishio, T. Morishita, W. Shinoda, M. Mikami, Molecular dynamics simulations of self-organized polyicosahedral Si nanowire. J. Chem. Physi., **125**, 074712 (2006)
49. J.F. Justo, R.D. Menezes, L.V.C. Assali, Stability and plasticity of silicon nanowires: the role of wire perimeter. Phys. Rev. *B*, **75** (4), 45303 (2007)
50. F. Glas, J.C. Harmand, G. Patriarche, Why does wurtzite form in nanowires of III-V zinc blende semiconductors? Phys. Rev. Lett., **99** (14), 146101 (2007)
51. Y. Zhao, Y.H. Kim, M.H. Du, S.B. Zhang, First-Principles prediction of icosahedral quantum dots for tetravalent semiconductors. Phys. Rev. Lett., **93** (1), 15502 (2004)
52. S.G. Hao, D.-B. Zhang, T. Dumitrică, Effect of small shape changes on the optical response of highly symmetric silicon quantum dots. Phys. Rev. *B*, **76** (8), 81305 (2007)
53. F.H. Stillinger, T.A. Weber, Computer simulation of local order in condensed phases of silicon. Phys. Rev. *B*, **31** (8), 5262–5271 (1985)
54. J. Tersoff, Modeling solid-state chemistry: interatomic potentials for multicomponent systems. Phys. Rev. *B*, **39** (8), 5566–5568 (1989)
55. H. Balamane, T. Halicioglu, W. A. Tiller, Comparative study of silicon empirical interatomic potentials. Phys. Rev. *B*, **46** (4), 2250–2279 (1992)

Springer

http://www.springer.com/978-3-642-12069-5

Trends in Nanophysics
Theory, Experiment and Technology
Aldea, A.; Bârsan, V. (Eds.)
2010, XVIII, 382 p. 164 illus., Hardcover
ISBN: 978-3-642-12069-5